https://doi.org/10.5194/egusphere-2026-2032
Preprint. Discussion started: 14 April 2026
© Author(s) 2026. CC BY 4.0 License.

# Calibrating JANUS: an overview of the calibration pipeline and what we learned from the Moon-Earth flyby data

Livio Agostini[1], Klaus-Dieter Matz[2], Cecilia Tubiana[1], Vincenzo Della Corte[3], Luca Penasa[4], Thomas Bilotta[5], Francesco Sarti[5], Matthew Read[6], Stubbe Hviid[2], Stefano Mottola[2], Alessio Aboudan[7], Frank Trauthan[2], Romolo Politi[6], Michael Aye[8], Ricardo Hueso[9], Alice Lucchetti[6], Elke Kersten[2], Ines Belgacem[10], Angela Dietz[11], Ry Evill[11], Jim F. Bell III[12], Angelo Zinzi[13], Jose Maria Castro Marin[14], Thomas Roatsch[2], Nicole Schmitz[2], Manish R. Patel[6], Luisa M. Lara[14], Ganna Portyankina[2], and Pasquale Palumbo[1]

[1]INAF - IAPS (Istituto di Astrofisica e Planetologia Spaziali), Via Fosso del Cavaliere 100, 00133, Rome, Italy
[2]German Aerospace Center (DLR), Institute of Space Research, Rutherfordstr. 2, 12489 Berlin, Germany
[3]INAF - OACN (Osservatorio Astronomico di Capodimonte), Salita Moiariello 16, 80131, Napoli, Italy
[4]INAF - OAPd (Osservatorio Astronomico di Padova), Vicolo Osservatorio 5, 35122, Padova, Italy
[5]Leonardo SpA, Via delle Officine Galileo 1, 50013, Campi Bisenzio (FI), Italy
[6]School of Physical Sciences, The Open University, Milton Keynes, MK7 6AA, UK
[7]Università di Padova - CISAS Giuseppe Colombo, via Venezia 15, 35131 Padova, Italy
[8]Freie Universität Berlin, Inst.for Geosciences, Malteserstr. 74-100, 12249 Berlin, Germany
[9]Escuela de Ingeniería de Bilbao, Universidad del País Vasco, UPV/EHU, Plaza Ingeniero Torres Quevedo 1, 48013 Bilbao, Spain
[10]European Space Agency (ESA), European Space Astronomy Centre (ESAC), Villanueva de la Cañada, Madrid, Spain
[11]European Space Agency (ESA), European Space Operation Center, Darmstadt, Germany
[12]Arizona State University, School of Earth and Space Exploration, Box 876004, Tempe, AZ, 85287,USA
[13]ASI (Agenzia Spaziale Italiana) - Centro Spaziale di Matera, C.da Terlecchia, 75100, Matera, Italy
[14]IAA-CSIC (Instituto de Astrofísica de Andalucía - CSIC), Glorieta de la Astronomía 3, 18008 Granada, Spain

**Correspondence:** Livio Agostini (livio.agostini@inaf.it)

**Abstract.** JANUS (Jovis Amorum Ac Natorum Undique Scrutator) is the high-resolution multispectral camera on board of the ESA Jupiter Icy Moons Explorer (JUICE). The mission, launched in April 2023, is currently traveling towards the Jovian system where it will characterize Jupiter, its environment and its icy moons, primarily Ganymede. During 19-20 August 2024 JUICE flew by the Moon and the Earth performing a Lunar-Earth Gravity Assist maneuver (LEGA) that provided a unique opportunity to test the instruments in mission-like conditions. In this paper we describe the status of the calibration pipeline applied to JANUS data acquired during LEGA, the lessons learned by the analysis of the calibrated data and the open points.

## 1 Introduction

One of the most important aspects of a scientific instrument is the calibration of the data. Calibration requires a deep knowledge of the instrument, which is acquired during years of development, laboratory testing, operation of the instrument and data analysis. Generally, this is an iterative process requiring multiple steps that converge towards a stable calibration procedure aimed at satisfying or exceeding the instrument accuracy requirements. For a space instrument, this process is particularly complex due to the strong constraints imposed by limited ground-testing opportunities under operational conditions and limited in-flight data volume. For JANUS (Palumbo et al., 2025), the high-resolution multispectral camera aboard ESA's JUICE (Grasset et al., 2013) mission, we took advantage of the periodic Payload Checkout Windows (PCW) to perform routine verification of the main properties of the camera.

The camera design, thanks to the presence of a cover module (COM) allows the execution of two types of tests: with COM closed or COM open, the latter allowing for observations of external sources. In this way, the dark current contribution, the radiometry and the optical stability can be routinely verified throughout the cruise phase. We defined some measurements that are repeated for each PCW to partially automate the performance verification process. We underline that JANUS does not have an internal calibration source.

On 19 and 20 August 2024, JUICE successfully completed the first ever Lunar and Earth Gravity Assist maneuver (hereafter LEGA) performing a close flyby of both targets and providing a unique opportunity to test the science payload capability in space environment and operating conditions similar to those expected during science phase when observing targets in Jupiter system. A detailed description of the planning of these acquisitions is provided in Tubiana et al. (this issue). Both Earth and the Moon are complex bodies observed by a large number of different sources making both excellent targets for verifying the capability of the calibration pipeline and to test the synergies between different instruments of the mission. We analyzed LEGA data with two main objectives: to validate and improve the calibration pipeline and to provide scientifically usable products. This approach requires multiple iterations to refine the quality of the data.

In this paper, we describe the current status of the JANUS calibration pipeline applied to LEGA data and the areas of improvement in which the JANUS team will focus during the cruise phase of the mission. A detailed description of the current calibration pipeline and how the products have been generated is not within the scope of this work and will be the topic of a dedicated paper.

## 2 JANUS camera

JANUS is the high-resolution scientific camera aboard the ESA JUICE mission. For a detailed description of the instrument, the reader is referred to Palumbo et al. (2025). Table 1 summarizes the high-level parameters for JANUS. In this section, we provide a technical description to help inform the calibration strategy.

The instrument is composed of three main parts:

- Optical Head Unit (OHU): hosts the instrument optics and focal plane, including the telescope, the filter wheel, the detector and the COM, providing light collection, image formation, and stable photodetection.
- Proximity Electronics Unit (PEU): drives and reads out the detector and performs the first stage of signal conditioning. The PEU includes the detector drive/clocking electronics, a compact analog front-end, the ADC, basic digital control and low-noise power conditioning, providing a streamlined electrical interface between the focal plane and the Main Electronics Unit.

**Table 1.** JANUS performance parameter. The radiometric F# is calculated considering the diameter of the effective collection area of the entrance pupil and not simply the geometrical one

| | |
|---|---|
| Focal length (nominal) | 467 mm |
| Pixel pitch | 7 µm |
| Focal Plane array | 2000 x 1504 pixels |
| Readout mode | Rolling shutter |
| Full frame readout time | 443 ms |
| IFOV | 15 µrad (3.1 arcsec) |
| FOV | 1.72° x 1.29° |
| F# (radiometric) | 4.58 |
| Bit depth (radiometric) | 14 bit |
| Exposure time range | 0.2215 ms to 113 s |
| Exposure time step (PEU tick) | 0.2215 ms |
| Spectral range | 340 to 1080 nm |

- Main Electronics Unit (MEU): Executes instrument control, data handling, compression, and interfaces with the spacecraft bus. It also provides instrument thermal control and generates the required secondary voltages.

The optical design is a modified Ritchey-Chretien telescope: a two-mirror catadioptric telescope with on-axis configuration. A filter wheel, placed before the detector, houses 13 filters allowing JANUS to observe from the near-UV to the near-IR (nominally from 340 to 1080 nm).

The detector (Teledyne e2v, 2017) is a 2000 x 1504 (rows x columns) pixels CMOS sensor with 7µm pixel pitch. Since it is a Back-side Illuminated (BSI) device, the fill factor is 100%. The detector implements a rolling shutter readout circuit meaning that the pixels do not integrate the signal simultaneously, with each row having the same exposure time and different start and stop times. Each row starts the integration with 1 tick delay from the previous row, where the tick is the clock unit of the PEU, which corresponds to 0.2215 ms. One consequence of the non-simultaneous exposure is the possibility of geometrical distortion, depending on the relative motion between camera and target (Liang et al., 2008).

The detector is read row-by-row by four different chains. Each readout chain manages 376 columns and includes a *REFERENCE* line, a *SIGNAL* line and a fully differential amplifier implementing a Correlated Double Sampling (CDS) operation. No delay exists between the four readout chains: each row has the same start/stop and no geometrical distortion is introduced in the row.

The signal is then digitized by a 14-bit Analogue-to-Digital Converter (ADC) and sent to the compression unit. JANUS can compress the data using a standard wavelet compressor, which allows both lossless and lossy compression.

Other useful features are the possibility to bin the pixels (binning) and have regions of interest (windowing), to reduce the data volume generated.

## 3 Radiometric calibration

### 3.1 General description

The radiometric calibration pipeline converts raw data intrinsic units (in DN, Digital Numbers) into physically radiometric units, that are spectrally integrated in the filter bandpass (in-band radiance), in units of $\mathrm{W\,m^{-2}\,sr^{-1}}$.

Figure 1 shows a sketch of the implementation of the current radiometric pipeline.

The fundamental calibration strategy approach is to consider each pixel as an independent detector. Therefore, if not explicitly stated, each step is considered to be performed at the pixel level. This approach is needed because of the intrinsic behavior of CMOS detector, where response non uniformity between pixels and non linearity vs. input signal prevent the application of a more traditional flat fielding technique. In addition, the JANUS detector is composed of 4 tiles, each with its own readout circuitry (as described in section 2).

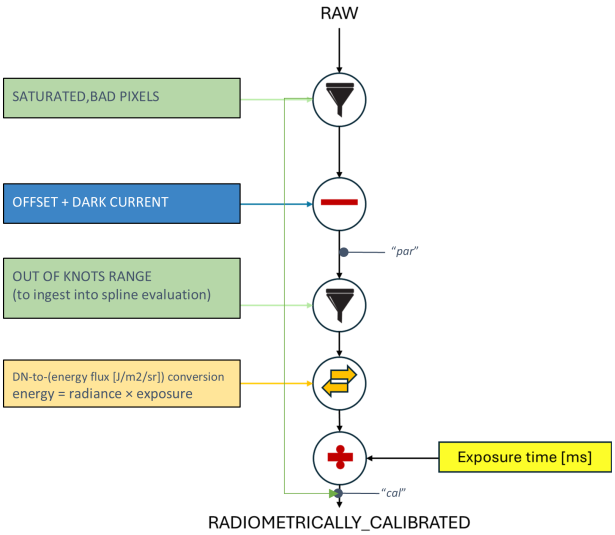

**Figure 1.** Schematic of the radiometric pipeline implementation for the analysis of the LEGA data. Inside the circular box it is shown the type of operation applied, in order: *filtering*, *subtraction*, *filtering*, *conversion* and *division*. The product levels nominally generated by the pipeline are also shown : *"raw"*,*"par"*,*"cal"*. Please note that the last three steps are all part of the module which convert data in absolute radiometric units. Here the internal steps of the module are shown for openness

The pipeline can also perform independent intermediate steps as needed and will nominally produce three types of products:

- raw data (DN units): images reconstructed from the telemetry files without processing; they are the digitized by detector readout.
- partially calibrated (*"par"*, DN units) : Offset and dark current subtracted. The saturation/bad pixel mask can optionally be disabled.
- calibrated (*"cal"*, W/m2/sr) : images with the full calibration pipeline applied.

An important aspect of the calibration procedure is that the pipeline can account for the evolution of instrument behavior, e.g., by applying a dark current correction based on the time of data acquisition. This ensures appropriate data quality, based on correct knowledge of the instrument behavior, during the mission. In the following subsections each step is described.

### 3.2 Saturation mask

The first step in the process is the detection of saturated pixels. This is based on a saturation-level map (Figure 2) determined during on-ground calibrations. The saturation level for each pixel is evaluated as the boundary value of the range where the derivative of the signal in DN with respect to the calibration proxy value (see section 3.5) is less than a threshold value, determined in a heuristic way. The raw data (background included) is compared pixel-per-pixel with the saturation map to generate a mask which is used to flag when a pixel is above its saturation level. For robustness reason, a pixel is considered *saturated* when it exceeds 98% of the corresponding pixel value in the saturation map.

The flagging is not static because it depends on the target radiance and acquisition parameters, such as integration time, and therefore it is determined for every image processed by the pipeline. The mask is computed as first step, but applied at the end, ensuring that the flag is present on the generated product.

### 3.3 Bad pixel mask

An analogous procedure is also used for bad pixels with the fundamental difference that bad pixels are *static* compared to saturated ones. Even if in principle bad pixel distribution can be different between images of the same session, their detection can be extremely challenging and the current adopted strategy is to apply the mask based on pre-determined bad pixel maps, with no active determination of new bad pixels by the pipeline itself.

On-ground calibration analysis showed that there were no bad pixels present. However, a new evaluation based on in-flight data acquired during PCWs suggests that future pipeline releases will regularly need to update the bad pixel map. Due to the negligible impact, for the time being no bad pixel mask was required for the LEGA data.

### 3.4 Offset and dark current subtraction

The first major processing step of the raw data is the removal of the electronic offset and the dark current. We decided to perform this operation in a single step using simulated images. For each image, the pipeline reads the detector temperature and the exposure time generating an image which is subtracted from the raw image. The first dataset was acquired in ground

© Author(s) 2026. CC BY 4.0 License.

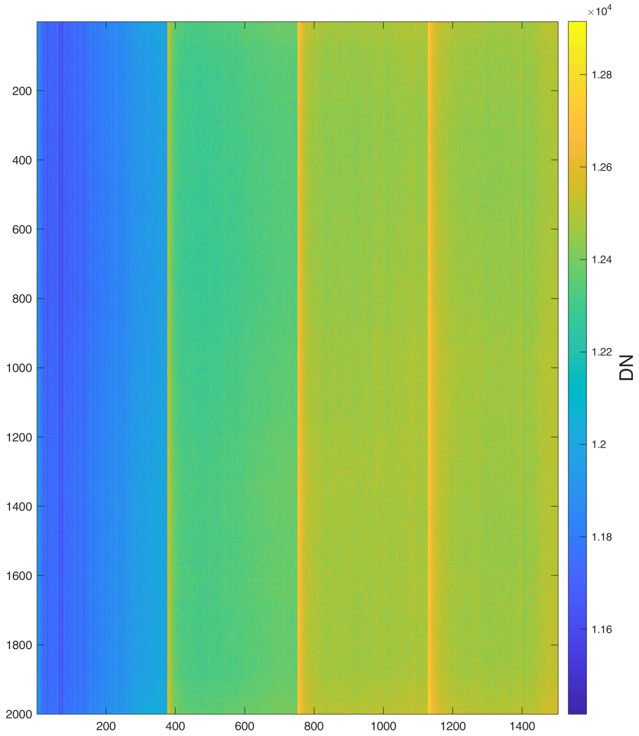

**Figure 2.** Saturation map for JANUS. The colorbar shows the value of the saturation in DN

tests, in dark and at different detector temperatures spanning the entire range of integration times. An extended dataset has been considered using in-flight data, taking advantage of data acquired during PCW opportunities, in particular from the Near-Earth Commissioning Phase (NECP) and PCW1 and PCW2. A new set of calibration factors has been generated that is more descriptive of the instrument behavior.

The instrument operated in a limited temperature range (the detector temperature varied less than 5°C), and to maintain the correction module as simple as possible, we used a simple multi-linear fitting, assuming linear dependence from both temperature and exposure time. For each pixel, we calculate the DN associated with its dark current and bias as:

$$\begin{aligned} DN_{dark} &= A \cdot t_{exposure} + B \\ A &= (x_1t_1 \cdot T_{detector} + x_1t_0) \\ B &= (x_0t_1 \cdot T_{detector} + x_0t_0) \end{aligned} \tag{1}$$

These four coefficients ($x_1t_1$, $x_1t_0$, $x_0t_1$, $x_0t_0$) are collected as maps of the same dimension of the image.

Figure 4 shows the average residuals of the fitting procedure applied to the large dataset mentioned before. The average is calculated separately for each of the four tiles which form the detector, and are displayed with different colors. Along with the residuals, the detector temperature and exposure time are shown. The fitting strategy worked well, providing for all the sessions a residual frame with average value ±1.5 DN (Figure 4).

https://doi.org/10.5194/egusphere-2026-2032
Preprint. Discussion started: 14 April 2026
© Author(s) 2026. CC BY 4.0 License.

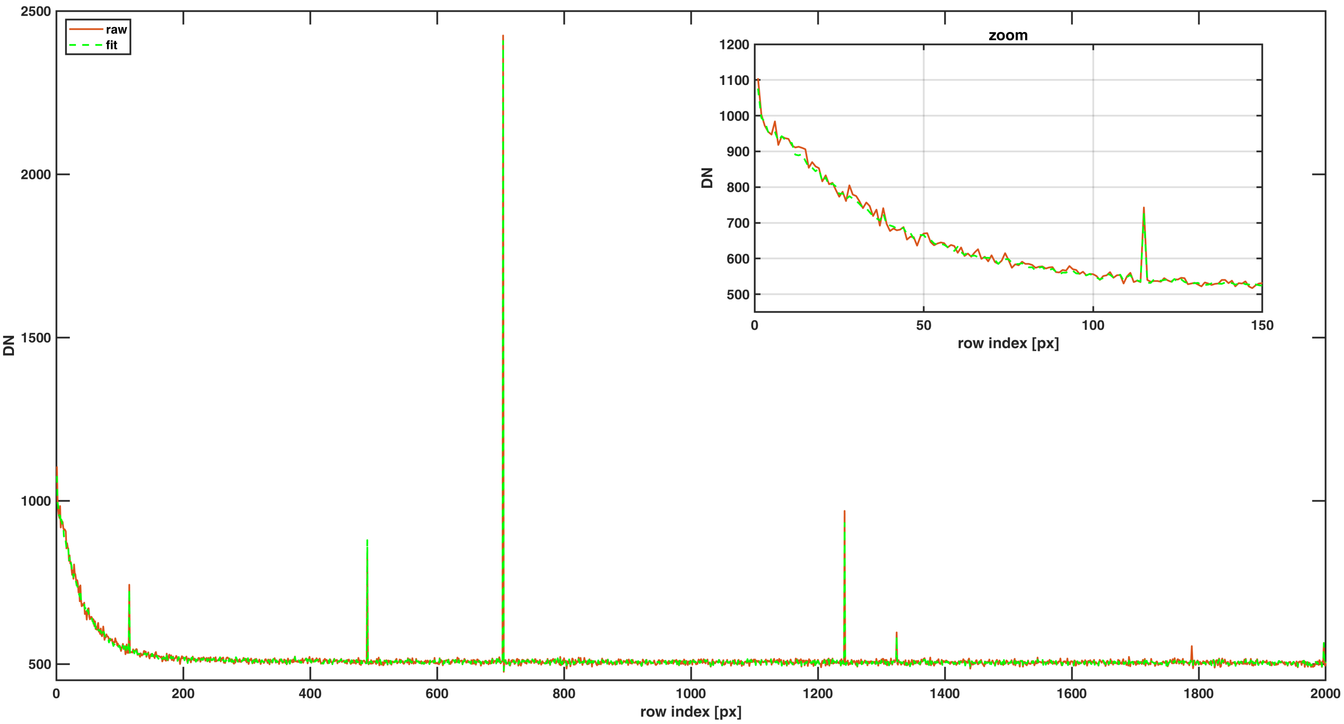

**Figure 3.** Profile of a raw image along the column identified by index 0 along with the simulated background. Hot pixels are visible as spikes. The detector temperature is -36.8C°, the exposure time is 113 s. Orange represents the raw data and the green dotted line represents the simulated profile.

The average contribution of the dark current is relatively small ($\leq$ 20 DN at -37°C at 113 s). For the longest exposure time used (113 s), the detector edge (Figure 3) experiences dark current values up to 600 DN, equivalent to about 5% of the saturation level.

### 3.5 Absolute radiometric calibration

The conversion from DN (background removed) to in-band integrated radiance is performed in two steps:

- evaluation of a proxy variable value from the signal in DN
- division of the proxy value by the exposure time

The proxy variable we used is the specific energy (radiance multiplied by the exposure time). The radiance has been calculated by integration of the calibration source spectral radiance over the bandpass of each filter. The calibration source has been calibrated against a calibrated spectroradiometer. The cut-on and cut-off wavelengths for each filter are part of the calibration dataset.

© Author(s) 2026. CC BY 4.0 License.

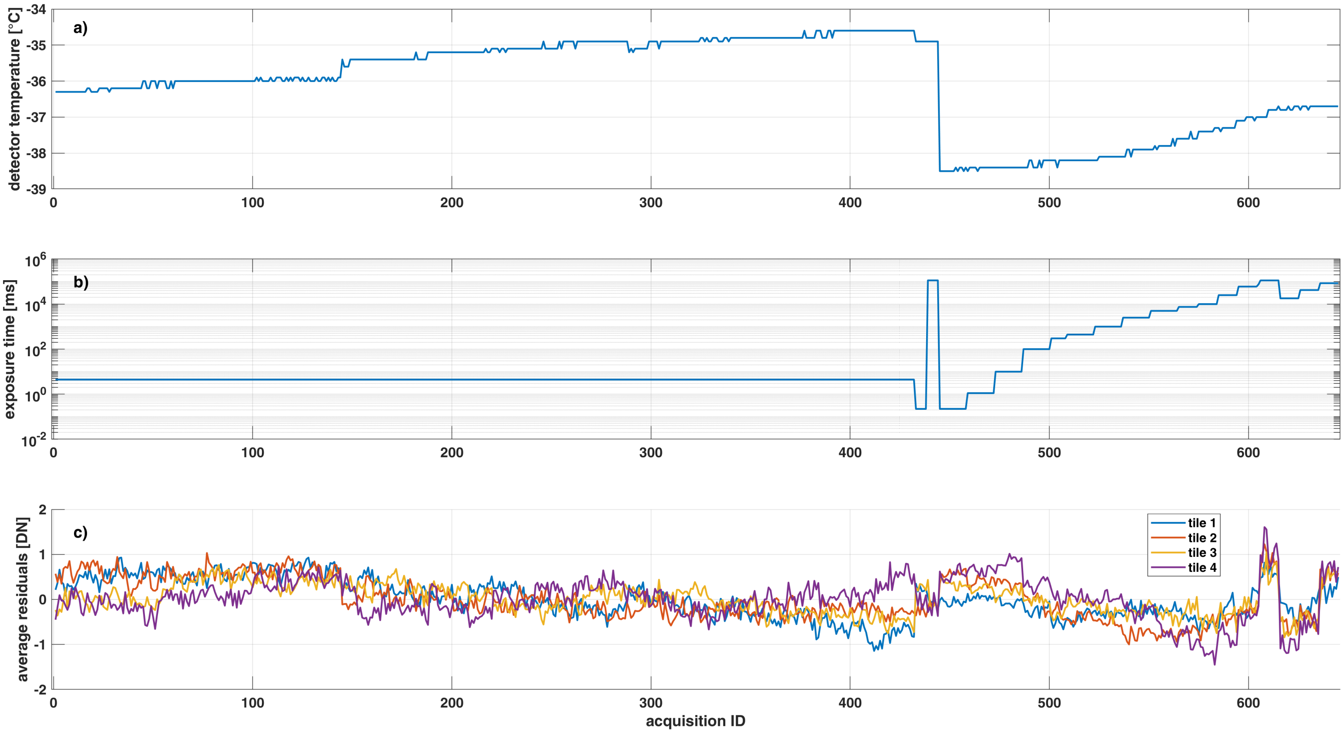

**Figure 4. a)**: detector temperature, **b)**: exposure time and **c)**: average of residual frame with respect to *acquisition ID*. The *acquisition ID* is the progressive enumeration of dark frames acquired by JANUS and used for the fitting. It can also be considered as a chronological record. The mean is computed independently for each of the four tiles.

The exact method and considerations used for the determination of calibration products are not the subject of this work and will be described in a dedicated publication.

The response of each pixel is fitted using a least-squares spline (Figure 5) using five polynomial pieces composed of cubic splines. The selection of the number of pieces has been driven by the need to be flexible enough to catch the non-linearity of the response but avoiding a huge amount of calibration products. It is important to note that with this approach, what is generally termed as 'flat-field correction' is already embedded to the procedure itself; therefore, its explicit application is not required. Moreover, this approach removes the need to choose at which level to calculate the flat-fielding matrix (for detectors not having a high degree of response uniformity). An example could be observed directly from Moon observation data. In Figure 6, the left image is partially calibrated and four vertical sections are clearly visible. The striping arises as a result of the slightly different gain of the four parallel readout chains from which the entire image is read. After calibration (right image of Figure 6), these artifacts are removed.

Another advantage is the possibility to extend the dynamic range in the non-linear region close to saturation. We observed that the calibration curves do not change at different temperatures, therefore we considered, for each pixel, only the dependence on the filter.

**Table 2.** JANUS filter bandpass definition, according to the radiometric calibration pipeline

| **Filter** | $\lambda_{avg}$ [nm] | $\Delta\lambda$ [nm] | $\lambda_{start}$ [nm] | $\lambda_{end}$ [nm] |
|---|---|---|---|---|
| 1 | 651.50 | 502.0 | 400.5 | 902.5 |
| 2 | 448.50 | 59.8 | 418.6 | 478.4 |
| 3 | 538.90 | 60.4 | 508.7 | 569.1 |
| 4 | 644.80 | 60.6 | 614.5 | 675.1 |
| 5 | 748.85 | 20.9 | 738.4 | 759.3 |
| 6 | 590.75 | 10.9 | 585.3 | 596.2 |
| 7 | 889.60 | 21.8 | 878.7 | 900.5 |
| 8 | 941.30 | 21.4 | 930.6 | 952.0 |
| 9 | 726.55 | 11.9 | 720.6 | 732.5 |
| 10 | 379.10 | 69.3 | 350.0 | 419.3 |
| 11 | 909.15 | 82.3 | 868.0 | 950.3 |
| 12 | 1014.95 | 132.1 | 948.9 | 1081.0 |
| 13 | 656.30 | 11.2 | 650.7 | 661.9 |

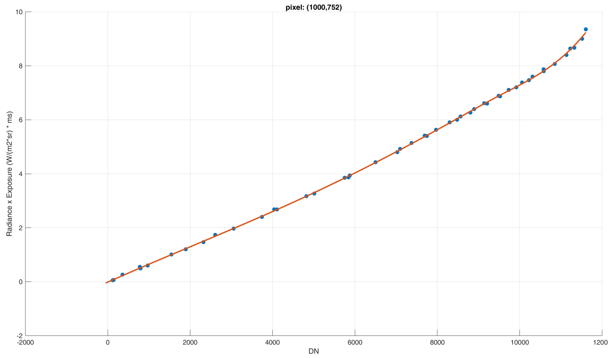

**Figure 5.** Example of the calibration curve for the boresight pixel of JANUS. The measurements refers to F1 (Panchromatic filter). In **blue** the experimental dataset, in **red** solid line is the result of the fitting

## 3.6 Post-radiometric correction

In the following two subsections we will describe the procedures that we have developed and applied on the data but not yet formally included into the pipeline. They will be a standard step in the next release.

https://doi.org/10.5194/egusphere-2026-2032
Preprint. Discussion started: 14 April 2026
© Author(s) 2026. CC BY 4.0 License.

Figure 6. Partially (left) and fully calibrated (right) version of the same image. The vertical striping, introduced by the readout electronics, are removed after the absolute radiometric correction module

### 3.6.1 Spectral correction

The *cal* level (which is the output of the previous section) is generated considering a calibration curve which converts from the DN (digital number) to the radiance (integrated in band); the calibration parameters were derived from laboratory measurements, where a calibrated light source has been used. Differences between the spectrum of the calibration source and the spectrum of the target implies that the calibration pipeline can give a slightly incorrect radiance. This is because two targets with different spectral shapes, but the same in-band integrated radiance, could give different signals on the detector because the latter depends on the product of the input spectral radiance and the Instrument Transfer Function (ITF), which is a function of wavelength. This is why results should be corrected for the spectral shape of the target under observation. The effective in-band radiance value is calculated as:

$$L_{target,filter} = S_{target,filter} \cdot L_{cal,filter} \tag{2}$$

$$S_{target,filter} = \frac{\dfrac{\int_{\lambda_i}^{\lambda_f} L_{calibration}(\lambda)\cdot ITF(\lambda)d\lambda}{\int_{\lambda_i}^{\lambda_f} L_{calibration}(\lambda)d\lambda}}{\dfrac{\int_{\lambda_i}^{\lambda_f} L_{target}(\lambda)\cdot ITF(\lambda)d\lambda}{\int_{\lambda_i}^{\lambda_f} L_{target}(\lambda)d\lambda}} \qquad (3)$$

where $S_{target,filter}$ is the correction factor, $L_{cal,filter}$ is the image generated by the absolute radiometric calibration step, $L_{calibration}$ is the spectral radiance of the calibration light source, $L_{target}$ is the spectral radiance of the target under observation, $\lambda_i$ and $\lambda_f$ are, respectively, the wavelength defining the cut-on and cut-off of the filter bandpass. From the equations, it appears that calculating this coefficient requires a priori knowledge of the target spectral shape (the absolute level is not required). For the Moon it is easier to determine and we have generated a set of coefficients ($S_{moon}$ in Table 3) that can be used to correct for the spectral difference introduced by the calibration lamp. For the Moon, we calculated a full disk irradiance spectrum using the LIME model (details in Toledano et al. (2024)). For the Earth, due to the high variability of spectral sources inside the same image (e.g. clouds, oceans, soil), this step is left to the user according the objective of their research. During the science operations phase, information from the MAJIS imaging spectrometer (Poulet et al., 2024), for example, could be used to compute the proper correction factors.

**Table 3.** Spectral correction parameters for the Moon

| filter | S_moon | C_filter | in-band solar irradiance [W/m$^2$] |
|---|---|---|---|
| 1 | 0.9586 | 0.0043 | 757.611 |
| 2 | 1.0084 | 0.0288 | 112.259 |
| 3 | 1.0060 | 0.0288 | 112.346 |
| 4 | 1.0020 | 0.0331 | 97.696 |
| 5 | 1.0004 | 0.1215 | 26.610 |
| 6 | 1.0019 | 0.1645 | 19.649 |
| 7 | 1.0009 | 0.1608 | 20.102 |
| 8 | 1.0018 | 0.1838 | 17.586 |
| 9 | 1.0008 | 0.2155 | 14.995 |
| 10 | 1.0469 | 0.0371 | 87.131 |
| 11 | 0.9975 | 0.0445 | 72.555 |
| 12 | 0.9839 | 0.0345 | 93.712 |
| 13 | 1.0048 | 0.1881 | 17.185 |

© Author(s) 2026. CC BY 4.0 License.

#### 3.6.2 I/F conversion

The I/F has been calculated using the following formula:

$$I/F = \frac{L_{target}}{\int_{\lambda_i}^{\lambda_f} E_{Sun}(\lambda) d\lambda} \cdot \pi \cdot d[AU]^2 \quad (4)$$

where $L_{target}$ is the in-band radiance as derived by spectral correction, $E_{Sun}$ is the solar spectrum and $d$ is the distance between the target and the Sun in astronomical units. The selected solar spectrum is the MODTRAN one, MCebKur model (retrieved in MODTRAN). The equation can also be written in the form:

$$I/F = S_{target,filter} \cdot C_{filter} \cdot L_{cal} \quad (5)$$

where $L_{cal}$ is the output of the current calibration pipeline (level *cal*) and $C_{filter}$ is a combination of in-band solar irradiance and distance (and $\pi$). For the Moon case, both coefficients are reported in Table 3.

## 4 Geometric calibration

### 4.1 General description

The other fundamental aspect that should be taken into account, in particular for a high-resolution camera, is the geometrical calibration. The objective is to have a function and/or algorithm able to map the intrinsically bidimensional information (in terms of position) on the detector in the 3D space. It is important to note that the radiometric calibration pipeline does not contain a rewarping step, in which the distorted image is re-mapped into an undistorted version of the same. The JANUS strategy is instead to provide the radiometric data along with the geometrical information. The geometrical information, stored in the relative *geocube* provides the relation between each pixel and its direction of sight, free of all distortions. The advantage of this choice is to avoid unnecessary multiple resampling of the image, which would degrade the resolution. In this way image resampling is only performed once during the very last step of the processing of the higher-level products, as projected maps and mosaics, and includes also all the necessary geometric corrections. In terms of geometrical distortions, two main contributions affect the raw JANUS data:

- optical distortion
- rolling shutter distortion

Optical distortion is related to the optical design and the effective alignment of the instrument components (including the filters in the filter wheel and the detector). Rolling shutter distortion, already described in the instrument description section, is related to *"when"* each row is acquired with respect to a target in motion. Given the very different nature of the two effects, they are treated separately.

© Author(s) 2026. CC BY 4.0 License.

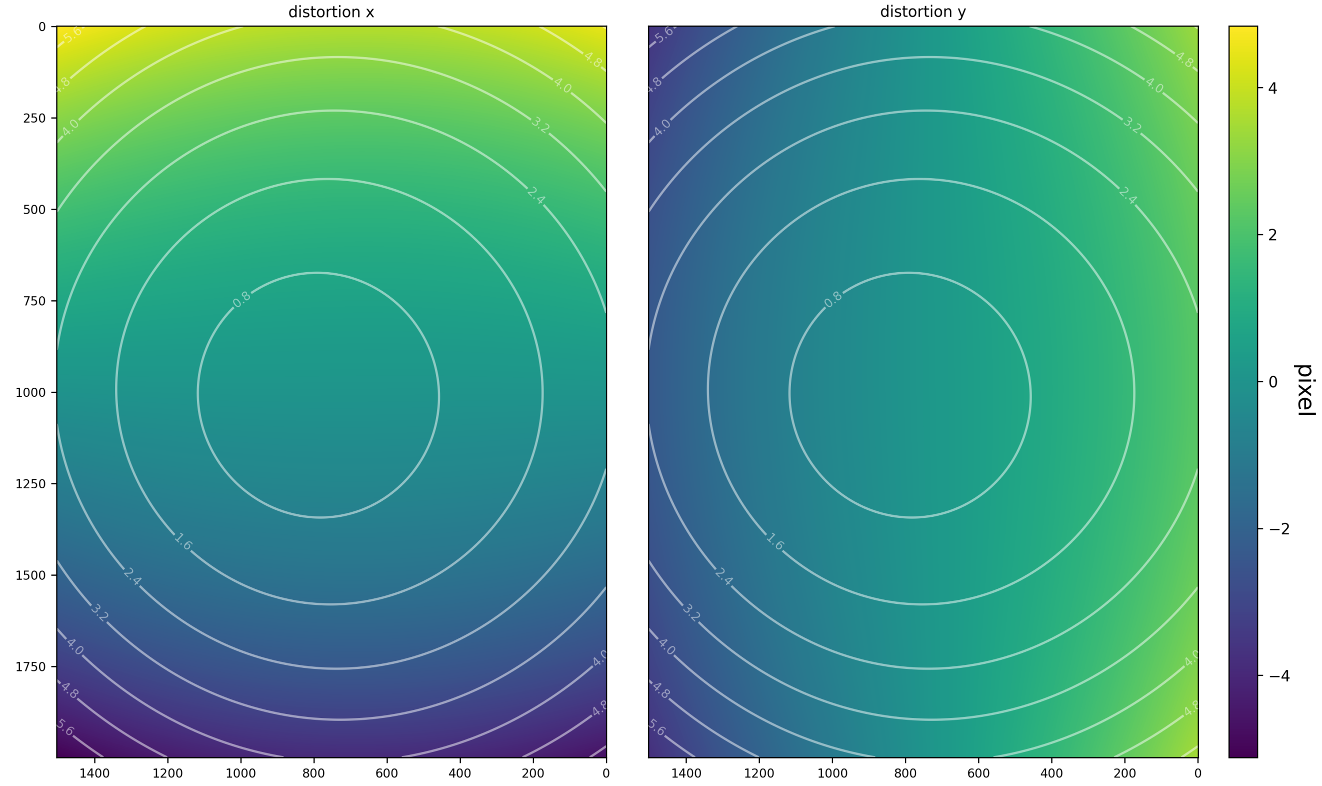

**Figure 7.** Current implementation of the optical distortion matrices, in x and y directions. These matrices show the maps of the ideal coordinates with respect to the distorted coordinates. To show the effective distortion, these plots display the difference in coordinates. The units of the distortion values are in pixel. In *white* are displayed the contours of the module of distortion vector in pixel units.

## 4.2 Parameters determination

In this section we describe how the optical distortion has been modeled and determined. The first consideration that has been taken into account is that JANUS is an on-axis camera, therefore a pinhole model is suitable as ideal reference model for the camera. This is described (Hartley and Zisserman (2004),Simioni et al. (2019)) by a combination of intrinsic matrix (which describes the first order geometrical parameter) and the extrinsic matrix (which describes how the camera reference system is oriented with respect to the world):

$$\begin{bmatrix} x \\ y \end{bmatrix}_{image} = hom^{-1}\left(\begin{bmatrix} f & 0 & cx \\ 0 & f & cy \\ 0 & 0 & 1 \end{bmatrix}\begin{bmatrix} R \end{bmatrix}\begin{bmatrix} X \\ Y \\ Z \end{bmatrix}_{world}\right) \tag{6}$$

where $f$ is the focal length (in pixels), R is the rotation matrix, $cx$ and $cy$ are the coordinates of the boresight and the $hom^{-1}$ is the inverse homogeneous operator. The real data are not described by this equation since it does not consider the distortions. The implemented strategy is a two-step process:

- determination of intrinsic/extrinsic parameters
- determination of distortion matrix

The first step is implemented with a non-linear least squares algorithm which seeks to minimize the cost function:

$$\sum_{i}^{N} |\boldsymbol{x}_{i,centroid} - \boldsymbol{x}_{i,model}| \tag{7}$$

Which corresponds to the euclidean distance between the (simulated) coordinates from ideal model described by equation 6 and the actual coordinates (that correspond to the distorted ones, measured by centroid determination). Thus, this step provides the orientation of the Instrument Line of Sight (ILS) with respect to, e.g., the JUICE reference system. In the second step, a bidimensional polynomial fit of undistorted coordinates (ideal model) with respect to the distorted ones is performed (Da Deppo et al., 2015). This is calculated for both $x$ and $y$ directions. As already described, JANUS performs some routine checks during the PCWs, some of the data are acquired with the COM opened. This permits observation of stellar fields that can be used as reference points for the fitting procedure. Since the release of the GAIA catalogue (Prusti et al. (2016), Vallenari et al. (2023)), the number of sources with very accurate astrometry has increased tremendously, making it easy to derive a dataset suitable for geometrical calibration. We developed an algorithm that, starting from a single image, queries directly the GAIA DR3 archive to derive the potential stars in the JANUS field of view. The star position is corrected for proper motion and for stellar aberration at the time of observation. In the same image the distorted coordinates of the star are determined by centroiding. For LEGA data, we decided to fix the coordinates of the boresight (in the middle of the detector, nominally [999.5,751.5] pixel, 0-based coordinate system) and the focal length to the nominal value (467 mm), allowing the algorithm to vary the angles which generate the rotation matrix. The distortion maps (Figure 7) are the final result of the analysis and strictly linked to the parameter settings used. The distortion map describes how many pixels (or millimeters) the coordinates of the ideal model are far from the distorted ones.

### 4.3 Geometric registration

The geometric registration pipeline (see Figure 8) is the part of the calibration process responsible for the generation of the geometrical products which come with the radiometrically calibrated data allowing the data to be correctly projected in space. For each pixel, starting from its coordinates, the viewing vectors are generated taking into account the distortion matrix. If an extended body is present in the instrument FOV, the intersection can be computed along with the illumination angles. Two types of products are generated from this pipeline:

- geocubes (*geo* level), multidimensional matrix with geometrical and illumination information

© Author(s) 2026. CC BY 4.0 License.

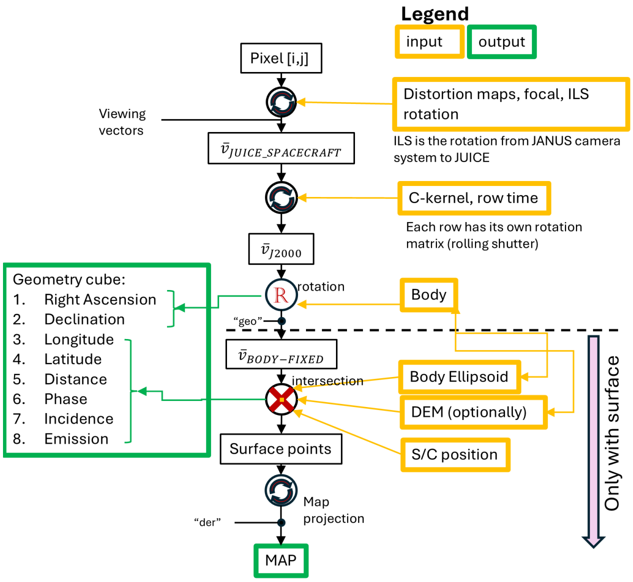

**Figure 8.** Schematic of the geometric pipeline implementation for the analysis of the LEGA data. Inside the circular box the type of operation applied is shown, in order: conversion, conversion, rotation, intersection, conversion. The product levels nominally generated by the pipeline are also shown : "geo","der"

- derived data ("*der* level), high level data containing the image projected on the selected surface coordinate reference system.

The structure of the geocube is described in Table 4. It should be noted that the first two planes of the cubes are always present because they describe the sight direction of each pixel in J2000 coordinates; the other planes only have valid values if the pixel line of sight intercepts the body. The algorithm has the capability of ingesting different reference surfaces which can be used to derive the intersection point of the sight direction on the surface. This is fundamental for LEGA data due to the fact that the phase angle was kept fixed at 90° due to the orbital design. This means that the parallax effect could not be neglected if accurate projection is required in particular towards the limb. Therefore, for the Moon data, we projected the data also using the Digital Terrain Model (DTM) from the Selene mission (Barker et al., 2016), which has a resolution of 60 m.

As already mentioned previously, the rolling shutter readout implemented by the JANUS detector introduces some distortion whenever the observing target is in motion with respect to the camera. The shape of the distortion depends on the direction of the relative velocity, and the amplitude of the distortion depends on the magnitude of the relative velocity.

The acquisitions of the Moon surface, for example, if no rolling shutter distortion is taken into account, would appear to be expanded. A visual description of this case is shown in Figure 9. The Figure shows a footprint of JANUS acquired 19 August during LEGA. The orange line shows the case where a global shutter would be implemented, i.e., all lines are captured simultaneously. The last row of the detector is acquired approximately 443 ms after the first row and since the spacecraft is moving towards the West; the last line is moving towards the West with respect to the last row of the global shutter case. The

© Author(s) 2026. CC BY 4.0 License.

**Table 4.** Structure of JANUS geocube

| Band | Parameter | Description | Unit |
|---|---|---|---|
| 1 | Right Ascension | View direction of pixel in J2000 | Degrees |
| 2 | Declination | View direction of pixel in J2000 | Degrees |
| 3 | Longitude | Eastern longitude of the intersection point on the target body | Degrees |
| 4 | Latitude | Planetocentric latitude of the intersection point on the target body | Degrees |
| 5 | Distance | Distance to the intersection point on the target body | Km |
| 6 | Phase Angle | Phase angle at the intersection point on the target body | Degrees |
| 7 | Incidence Angle | Incidence angle at the intersection point on the target body | Degrees |
| 8 | Emission Angle | Emission angle at the intersection point on the target body | Degrees |

amount of compression evaluated considering the ratio between the frame time (443 ms) and the repetition time (defined as the time required to cover the entire FOV) is shown in Figure 10.

This step of the geometric calibration pipeline corrects the rolling shutter distortion by calculating the sight direction at the effective time of the row. The optical properties are assumed to be the same at every time, but the position and attitude can change between one row and the following ones. Another point to highlight is that the determination of the distortion matrix has been done through star field observations while the spacecraft was in inertial pointing; therefore no rolling shutter distortion is expected.

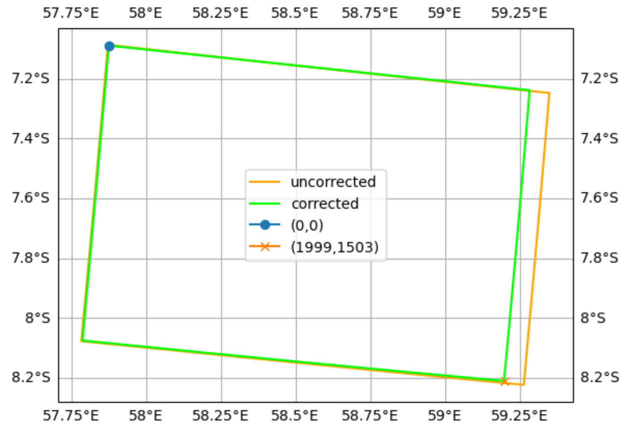

**Figure 9.** Example of rolling shutter distortion effect in the Moon data. In *orange* is the uncorrected case (analogous to global shutter case), in *green* the corrected projection (rolling shutter). The spacecraft is moving Westward.

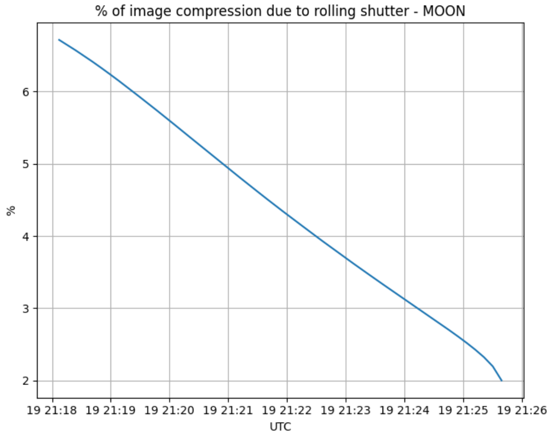

**Figure 10.** Estimation of the percentage compression introduced by the rolling shutter distortion in Moon data

## 5 Open Points

In this section we report the open points, the drawbacks and the lessons learned from the analysis of the LEGA data. They cover all the relevant aspects of the calibration and we are currently studying a correction strategy to be implemented in next release.

© Author(s) 2026. CC BY 4.0 License.

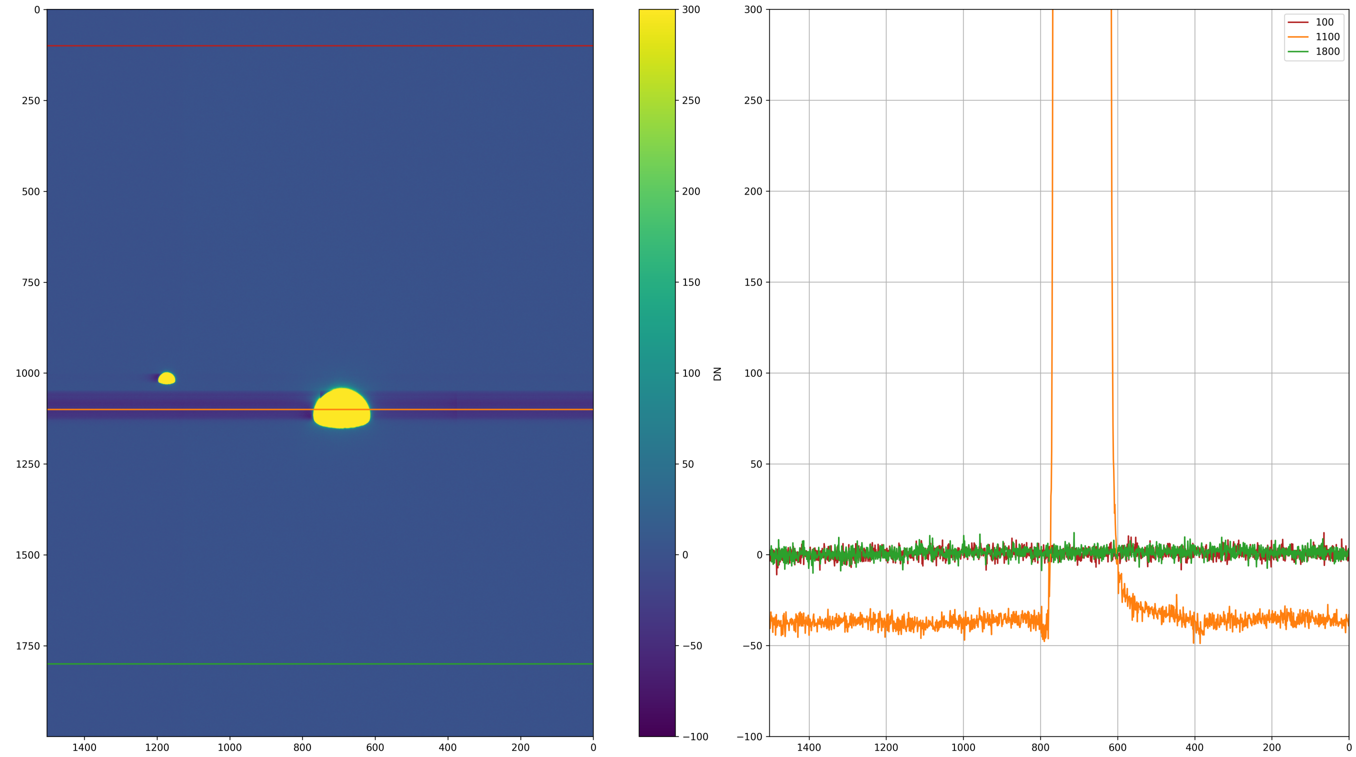

**Figure 11.** Example of the Signal Dependent Baseline Shift behavior in the Earth-Moon portrait. The orange line shows signal that is saturated in the illuminated zone to highlight the SDBS effect. **Left** partially calibrated image, with the colourbar scale ceases at 300 DN to better display the effect. The SDBS is visible as horizontal strips. **Right**: profile of the selected lines. The blue and green lines report a 0 signal because no illumination is present on those lines. The orange line shows instead a negative baseline due to the SDBS

## 5.1 Radiometric calibration

### 5.1.1 Signal Dependent Baseline Shift (SDBS)

It has been observed that when a signal is present on the detector, all the pixels having the same row index of an illuminated pixel, experience a shift of the expected signal towards negative values (see Figure 11). The magnitude of this effect depends on the overall signal in the same row in a linear manner up to saturation. For a generic target, the visual effect is the presence of relatively darker horizontal stripes across the detector in the region defined by rows which are illuminated.

Correction of this effect could be problematic in a windowing operation which excludes rows containing illuminated portions of the detector, because it causes an incomplete recovery of the information. A correction algorithm is being developed for future implementation in the pipeline. For the time being, referring to the image shown, we notice that this effect is relatively small when compared with the saturated signal level from which it is generated (less than 0.3%). On the other hand, it may give larger relative errors in absolute calibration when faint and bright sources are present in the same field.

© Author(s) 2026. CC BY 4.0 License.

### 5.1.2 Signal Baseline Gradient - SBG

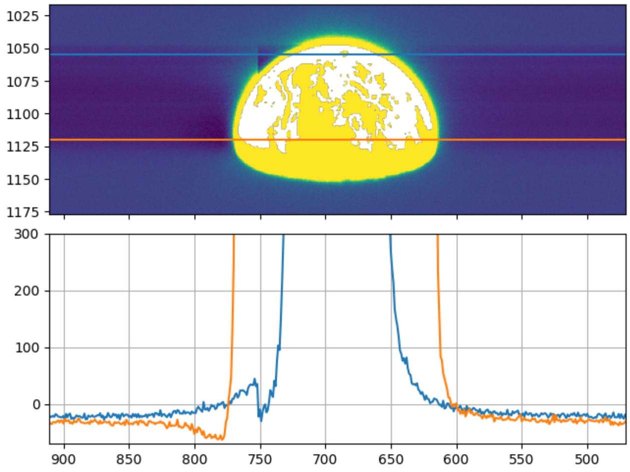

**Figure 12. Top**: Picture of the Earth showing the Signal Baseline Gradient. The image corresponds to an acquisition with the panchromatic filter (F1) and a exposure time of 0.2215 ms. The image is partially calibrated and the saturation mask applied. The colourbar scale is between -70 and 300 DN. **blue line**: profile of row 1120. About half of the illuminated columns are saturated. **orange line**: profile of row 1055. In this case all the illuminated columns are saturated.

The analysis of the SDBS showed another effect related to an illuminated source in a dark background. Figure 12 shows a picture of the Earth with two signal profiles. The image is partially calibrated (offset and dark current are removed) and the saturated mask is applied to show the actual boundary of the Earth. The orange line is a horizontal profile of row 1120. As expected the SDBS is present for all the columns, in this situation with a deviation of about 25 DN with respect to the 0. The additional effect we want to highlight can be seen in the column range 770 to 830, where a gradient appears to be present from about -60 DN at the most negative peak to the -25 DN of the SDBS. This gradient is present in general for column indices greater than the illuminated ones, i.e. on the left of the bright pixels in the figure. The source of this effect is not yet understood and it is under evaluation for appropriate correction.

We also want to report that row 1055 shows an abrupt change of signal continuity between columns 751 and 752. This is even more clear observing the sawtooth pattern on the top left part of the Earth. It should be noted that due to the clipping in the image, the actual boundary of the Earth is smaller than observable in the image, which also shows the diffusion and scattering due to the heavily saturated image. The boundary 751/752 column index identifies the separation between two different detector tiles and readout chains and it appears that the effect on the signal is limited to the illuminated tile and do not propagate to adjacent ones. We have not yet performed any investigations into this and it is not currently known whether it is related to the Signal Baseline Gradient effect, and it is reported for completeness.

The effect of SBG on the accuracy of radiometric calibration seems to be lower than for SDBS, also because it impacts a smaller detector area. It is more important for accurate analysis of images showing sharp radiance edges, such as limbs.

© Author(s) 2026. CC BY 4.0 License.

### 5.1.3 Straylight and Ghost analysis

One of the main open points for the radiometric calibration pipeline is the removal of ghost/straylight effects. The term *straylight* is used to describe unwanted light that reaches the focal plane of an optical system (Fest, 2013). Sources of straylight could be reflections from opto-mechanical surfaces, edges of optical components, etc. The term *ghost* identifies structures usually coming from in-field sources, from multiple reflections on the optical elements themselves, if at least one refractive element is present (Fest, 2013).

Specific measurements of those contributions have been considered in the acquisition plan for the LEGA with the basic idea to 1) have a quantification of the magnitude of the contribution and 2) have a suitable dataset to use as a comparison in a simulated numerical model.

An example of measurement of straylight contribution is displayed in Figure 13. From Figure 14 it is possible to see the geometry of the observation. The illuminated surface of the Moon is seen from JANUS with a considerable solid angle; this is an important condition because in-field, near-field and out-of-field straylight contributions are all then present in these images.

A rough estimation of the straylight contribution is about 20/50 DN over 7000 DN of the illuminated surface, that is 0.29-0.71 %.

It is also observed that when the exposure time is increased, a potential straylight pattern is revealed. Figure 15 shows an image acquired about 6 minutes after the image in Figure 13, so that the baffle is still illuminated (out of field) by the Moon. Here, a structure with concentric circumferences is clearly visible. We believe that they originate from straylight reflections from the internal vanes of the external cylindrical baffle. With similar considerations of the previous case, considering the same signal on the surface (7000 DN), the difference in exposure times (10000 $\mathrm{ms}$ with respect to 0.2215$\mathrm{ms}$) and the highest straylight signal of this image (about 3800 DN) the amount of straylight contribution is about 0.0012% which is compatible with the fact that only out-of-field straylight is present.

The third case we present is shown in Figure 16. In this situation the main source, the Earth, is over-saturated to raise the signal from multiple reflections of the primary mirror on the optical elements. The structure of the spider, which holds the secondary mirror in place, can be seen in the form of dark lines arranged at an angle of 120°. Due to the three-arm structure of the spider, the PSF pattern is expected to have six diffraction spikes. It should be noted that the horizontal spikes are superimposed on the SDBS-affected rows.

Even in this situation a rough estimation of the magnitude of the ghost contribution can be made. Considering that at 0.2215 ms, the same source in the same filter of Figure 16 is almost all saturated, at about 12000 DN, the level is <0.0083%.

An analysis based on ray-tracing simulation using the FRED software (Photon Engineering, LLC, 2026) is currently ongoing (Munari et al., 2024) to simulate these effects and define a correction strategy to be implemented in the next releases of the radiometric calibration pipeline.

© Author(s) 2026. CC BY 4.0 License.

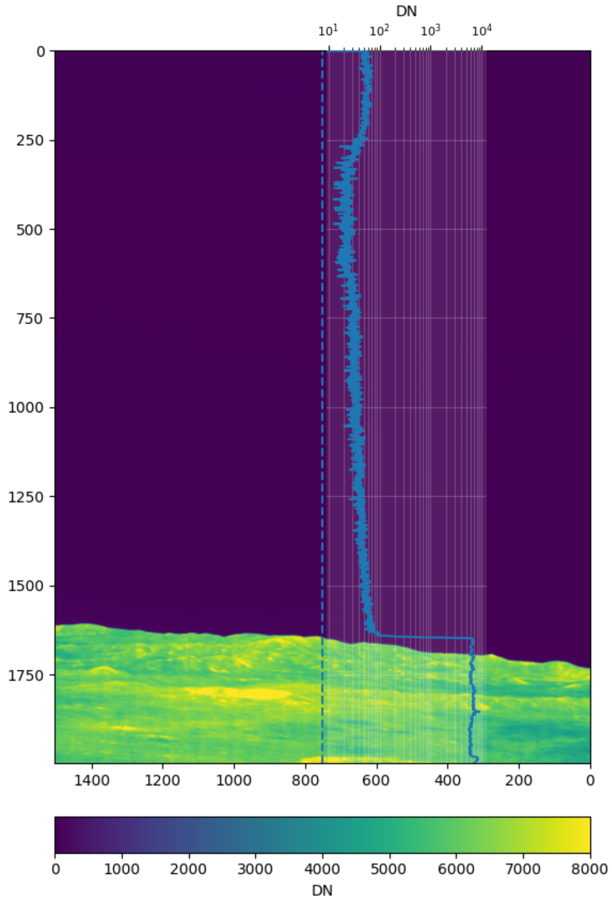

**Figure 13.** partially calibrated image. Exposure time: 0.2215 ms, Filter: 1. The image includes also a vertical profile in logarithm scale of the central column to show the straylight contribution. The acquisition is few seconds after the limb crossing and therefore includes, near-field, in-field and out-of-field straylight. The colourbar scale ceases at 8000 DN for improved visualization.

### 5.1.4 Radiometric calibration of very low signals

The result of the current implementation of the fitting procedure provides a smooth behavior up to the desired extension of the dynamic range (see for example Figure 5), even though no particular constraints have been imposed to the fitting procedure itself. However, the procedure results in some drawbacks for very low signals.

Assuming a perfect background correction, the zero observed signal should equal the zero 0 DN signal, in terms of average behavior. From Figure 17 it is clear that this is not always the case, and a slightly negative signal is produced by the pipeline, leading to a peculiar pattern which is an artifact from the pipeline itself (Figure 18).

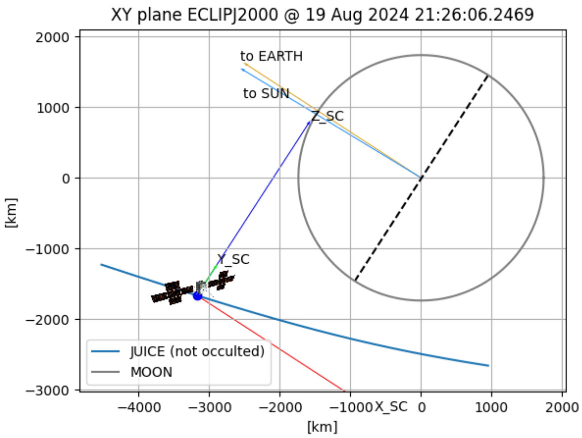

**Figure 14.** Pictorial representation of the observation geometry of Figure 13.

This could be problematic for analysis of sources with low signal or areas surrounded by low signals such as a star field on the terminator side of the LEGA data. We are reviewing the causes of this problem and we plan to provide corrected calibration products in the next release.

### 5.1.5 Diffusion

As already observed during the on-ground calibration campaign, the observation of the Earth-Moon system at a distance confirmed that the detector suffers from diffusion at longer wavelengths (and therefore in some subset of reddish filters).

Two images are reported: Moon observed using the F3 filter (539 $\mathrm{nm}$, Figure 19) and the same observation with F12 (1015 $\mathrm{nm}$, Figure 20).

The images have been chosen to have similar signals on the horizontal/vertical profiles (Greenish-blue lines in Figures). The coordinates of the profiles correspond to the JANUS-Moon center direction as derived using the ESA SPICE operational kernels without any additional corrections and projected on the JANUS detector. Both images correspond indicatively to the same longitude/latitude. The images have been plotted using asinh scale to show the entire dynamics and without excluding the negative values.

In the case of F12, a halo surrounds the Moon with a cross-shaped form in the row and column directions. It should be noted that the rows with coordinates greater than 1048 suffer from the SDBS generated by the Earth. In Figure 20 the diffusion is also propagating in this region.

A rough estimation of the relative impact of this effect is also reported, considering the pixel dimension of the region containing signal >10% of the maximum profile value, separately for horizontal and vertical cases (orange dotted lines in Figures 19 and 20). In the case of Figure 19 this region almost corresponds to the lunar geometrical shape, with steep edges. For Figure 20 the edges are smoother and significantly higher than the F3 case. This could be the result of diffusion in bottom

https://doi.org/10.5194/egusphere-2026-2032
Preprint. Discussion started: 14 April 2026
© Author(s) 2026. CC BY 4.0 License.

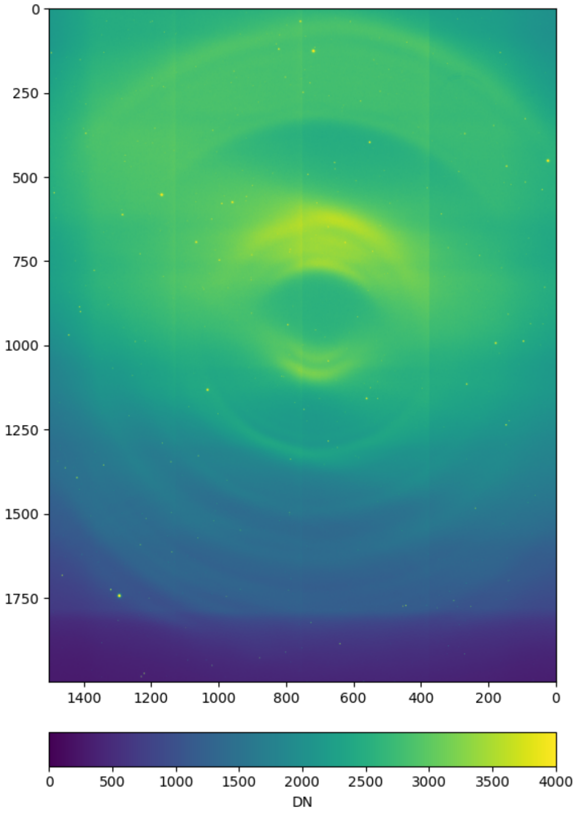

**Figure 15.** partially calibrated image. Exposure time: 9999.848 ms, Filter: F1. A straylight pattern is clearly visible as concentric circumferences. The colourbar scale ceases at 4000 DN for improved visualization.

part of the detector substrate, since it is known that QE degradation occurs at longer wavelengths where the silicon becomes more transparent due to the sensitive silicon thickness (Soman et al., 2014). This will be investigated further in future work.

### 5.1.6 Bandwidth relative errors

The current implementation of the algorithm that produces the calibration products performs a numerical integration of the spectral radiance sampled at 1 $\mathrm{nm}$. Although it is expected that for broadband filters (e.g. F1, F2, F3, F4) this accuracy is enough to produce reliable results, for narrowband filters with a nominal bandwidth of 10 $\mathrm{nm}$ the sampling is of the order of 10% of the bandpass. We explore the possibility to test calibration products generated with interpolated versions of spectral radiance of the calibration source, to have a refined version of the filter bandwidths. The spectral range calculated using a linear interpolation (sampling 0.1 $\mathrm{nm}$) is reported in Table 2. To have an idea of the impact on the radiometric calibration,

© Author(s) 2026. CC BY 4.0 License.

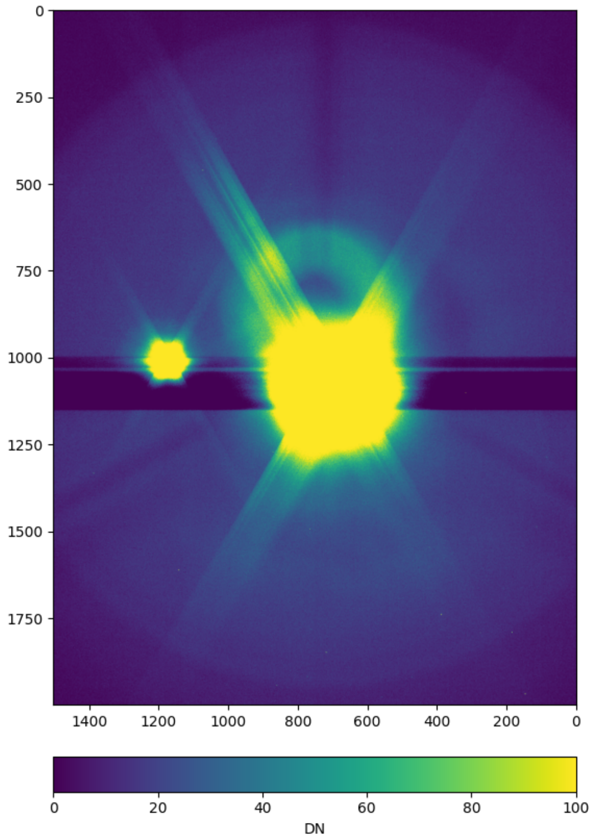

**Figure 16.** Partially calibrated image. Exposure time: 22.15 ms, Filter: F1. Ghost structures are visible as multiple reflections of the primary mirror. The colourbar scale ceases at 100 DN for improved visualization.

Table 5 reports the difference in the determination of the filter spectral range determined using linear interpolation with respect to spectral ranges used to generate the calibration products

In principle, even if no difference is present in the bandwidth dimension, an error could be also introduced by the absolute values of the cut-on and cut-off wavelengths. This error depends on the calibration spectrum and affects the narrowband filters to a larger extent. Here, we do not perform an estimation of that impact. Lastly, the dependence on incidence angle can not be neglected for the narrowband filters. For example, Figure 21 shows the transmittance of F6 at different incidence angles, which correspond to the angles of the cone of rays impinging on the detector (see Figure 6 of Palumbo et al. (2025)). It should be noted that in the optical design of the instrument the filters do not experience a collimated beam but a convergent one; this implies a range of incidence angles, which in turn affects the bandwidth position. The effective bandwidth is not the direct envelope considering all the possible incidence angles but should be weighted by the contribution to the signal. These effects have not been fully examined yet and their impact in the calibration will be considered in next releases of the calibration pipeline.

© Author(s) 2026. CC BY 4.0 License.

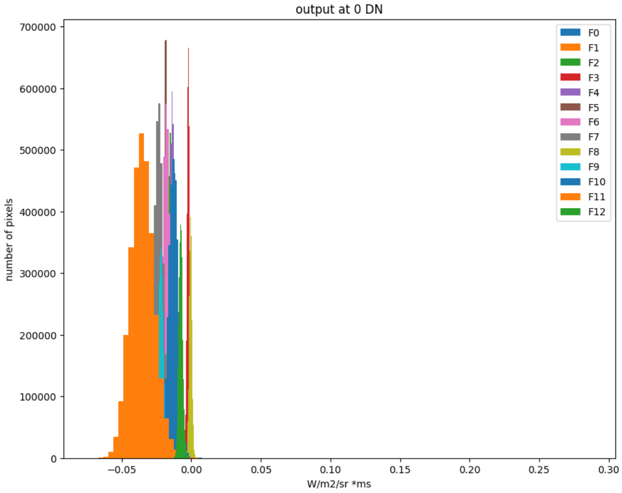

**Figure 17.** Histogram of the absolute radiometric calibration module output in response to a uniform signal of 0 DN. Each color is a different filter, as indicated by the legend.

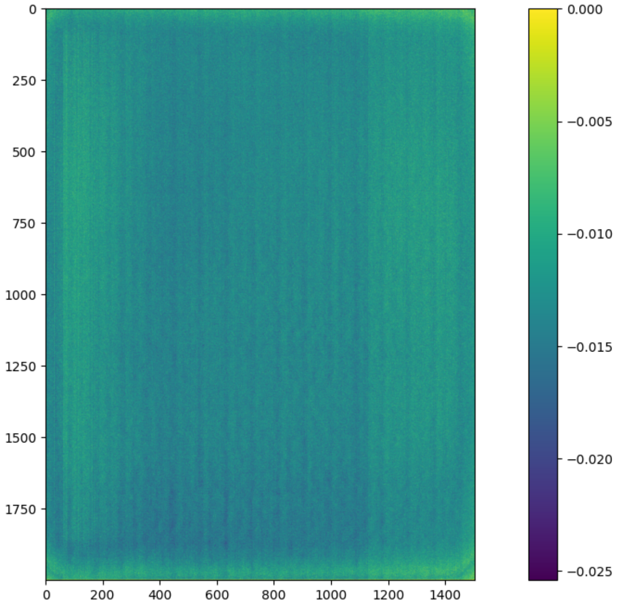

**Figure 18.** Image of the output of the absolute radiometric module using a uniform input of 0 DN for the filter F1. The value range has been limited to a maximum value of 0 to improve the visualization.

https://doi.org/10.5194/egusphere-2026-2032
Preprint. Discussion started: 14 April 2026
© Author(s) 2026. CC BY 4.0 License.

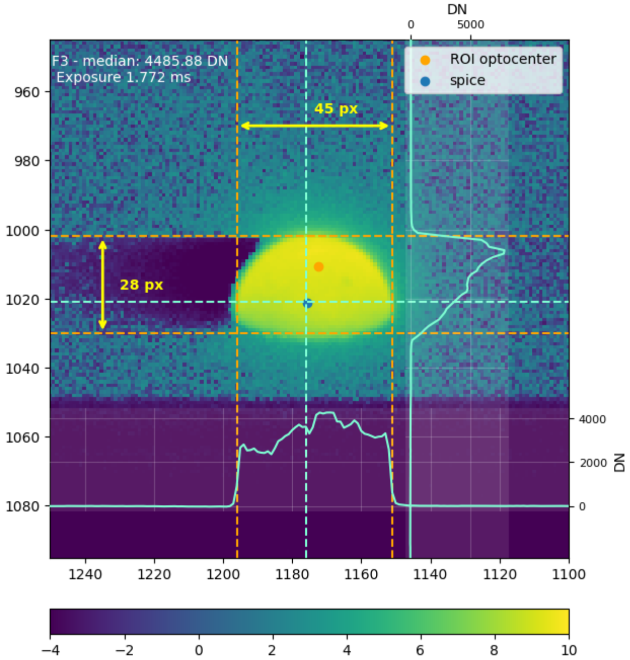

**Figure 19.** Moon observed in F3 filter in asinh scale. Greenish-blue profiles correspond to the signal intensity along the dotted lines of the same color. Orange lines define where the signal is >10% of the maximum profile value. Profile coordinates correspond to the JANUS-Moon center direction. The median value corresponds to the median of the values higher than 2000 DN in the ROI considered.

### 5.1.7 Systematic errors of the radiometry

Due to limitations in the ground calibration facility, our knowledge of the calibration spectrum in the F10 spectral range is limited to 350 $\mathrm{nm}$ while the filter cut-on is around 340 $\mathrm{nm}$. This causes an underestimation of the radiance. We did not extrapolate the spectral radiance of the calibration source out of the measured range, to avoid introducing systematic errors. In a future release, we will address this limitation.

Current efforts are focused on a systematic review and verification of the absolute radiometric calibration. However, some comparisons are already available for both the Moon (Langevin et al., this issue) and the Earth (Hueso et al., this issue), although the results are not yet definitive.

### 5.1.8 Low Exposure Time Response

During ground calibration we observed that at low exposure times the detector shows higher response than expected from other measurement conditions. To evaluate the instrument radiometric response we performed two types of measurements: fixed radiance level with variable exposure time and fixed exposure time with variable radiance level. Those measurements are combined, for each filter, into a single dataset using the proxy variable of the specific energy (as already mentioned in section

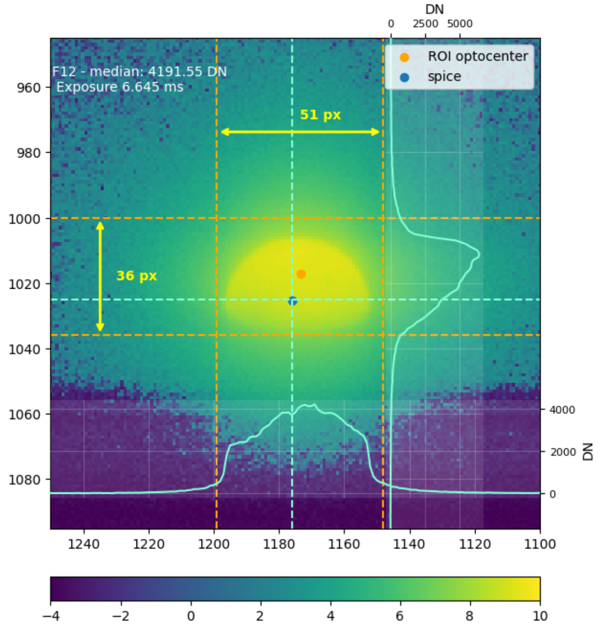

**Figure 20.** Moon observed in F12 filter in asinh scale. Greenish-blue profiles correspond to the signal intensity along the dotted lines of the same color. Orange lines define where the signal is >10% of the maximum profile value. Profiles coordinates correspond to the JANUS-Moon center direction. The median value corresponds to the median of the values higher than 2000 DN in the ROI considered.

3.5). The results for some example filters are reported in Figure 22. Additional details will be reported in future work, but until then the reader is referred to Agostini (2023).

For both F4 and F9 it is possible to observe a unique behavior for all the measurements, without dependence on exposure time, radiance or temperature setpoint. For F1, two curves are clearly observable, one for the measurements using fixed exposure time and varying the radiance and one for fixed radiance and varying the exposure time. A notable exception occurs for the measurements acquired at the *COLD* setpoint. The nominal *ITF vs Radiance* has been replicated but with an exposure time higher than nominal (16 $\mathrm{ms}$ instead of 0.88 $\mathrm{ms}$). For the case of the higher exposure time, the curve generated is in agreement with all the *ITF vs Texpo* sessions, which are in turn aligned with our radiometric model. Since low exposure times were only tested using F1, we suspect that some source of non-linearity is affecting the ITF at very low exposure times. We observed a similar behavior in in-flight measurements, suggesting that for exposure times $< 1.5$ $\mathrm{ms}$ the radiance is overestimated by the radiometric calibration pipeline. We are currently investigating the cause to determine the appropriate correction of the calibration strategy.

© Author(s) 2026. CC BY 4.0 License.

**Table 5.** Difference on wavelengths using linear interpolation (0.1 $\mathrm{nm}$ sampling) with respect to the default wavelength range (1 $\mathrm{nm}$ sampling, used the generation of the radiometric calibration products). Columns report the difference in absolute values with the exception of $\Delta\lambda$ which instead indicates a relative error (%)

| **Filter** | $\lambda_{avg}[nm]$ | $\lambda_{start}[nm]$ | $\lambda_{end}[nm]$ | $\Delta\lambda[\%]$ |
|---|---|---|---|---|
| 1 | 0.00 | -0.50 | 0.50 | 0.1996 |
| 2 | 0.00 | -0.40 | 0.40 | 1.3559 |
| 3 | -0.10 | -0.30 | 0.10 | 0.6667 |
| 4 | -0.20 | -0.50 | 0.10 | 1.0000 |
| 5 | -0.15 | -0.60 | 0.30 | 4.5000 |
| 6 | -0.25 | -0.70 | 0.20 | 9.0001 |
| 7 | 0.10 | -0.30 | 0.50 | 3.8095 |
| 8 | -0.20 | -0.40 | 0.00 | 1.9048 |
| 9 | 0.05 | -0.40 | 0.50 | 8.1818 |
| 10 | 0.10 | -0.10 | 0.30 | 0.5000 |
| 11 | 0.15 | 0.00 | 0.30 | 0.3659 |
| 12 | -0.05 | -0.10 | 0.00 | 0.0758 |
| 13 | 0.30 | -0.30 | 0.90 | 12.000 |

## 5.2 Geometrical calibration

### 5.2.1 Temperature dependence

It is known from STOP (Structural Thermal Optical Performance) analysis (Turella et al., 2019) and from laboratory measurements (Turella et al., 2021) that a variation of the thermal gradient between the Baffle Wall and the Optical Wall gives rise to rotation of the instrument boresight around the y axis. Figure 23 depicts the Baffle Wall and Optical Wall and the y-axis around which the above-mentioned rotation is experienced. Analysis suggest this is the dominant effect among other thermal effects that may play a role in the modification of the JANUS orientation with respect to JUICE. Baffle and Optical Walls support the baffle and the telescope, respectively; they can affect JANUS orientation because they also support the bipods used to mount the instrument on the spacecraft optical bench. In principle this effect can be taken into account and corrected by using the model described by Turella et al. (2021).

Other potential effects not currently included in this first release may come from the variation of the optical parameters produced by the differential displacement between the optical elements. Taking advantage of the following PCW opportunities, we plan to improve our knowledge of the instrument behavior under different thermal conditions. Eventually, calibration products and distortion maps will be related to a reference temperature and/or temperature gradient and the temperature itself will be used as a calibration input variable.

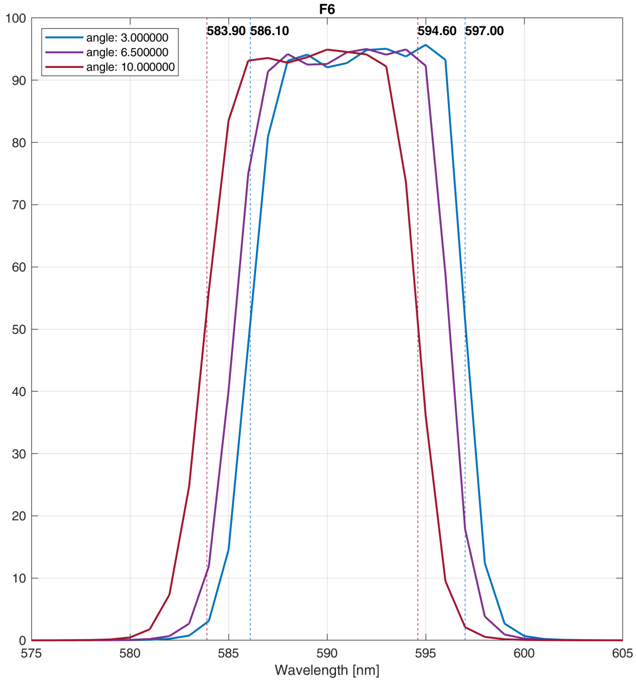

**Figure 21.** Transmittance of F6 filter at different incidence angles. Dotted lines show the wavelengths where the value is 50%

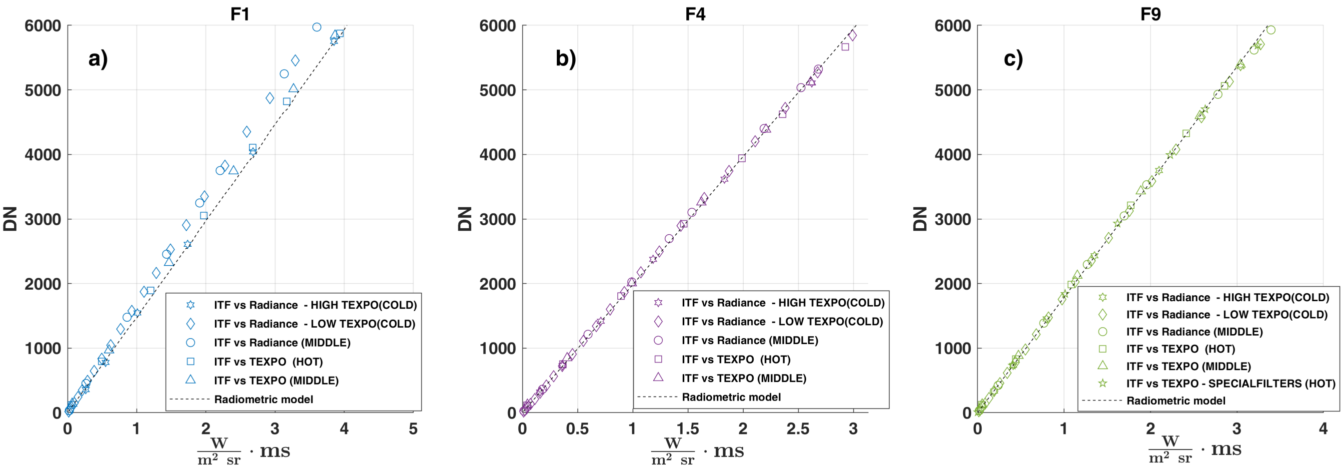

**Figure 22.** Example of radiometric response of JANUS during different calibration session. On x-axis there is the proxy value as described in section 3.5, on y-axis the DN. Three filters are reported as representative of filter categories on board JANUS: a) F1 (panchromatic), b) F4 (broadband filter) and c) F9 (narrowband). Each measurement is indicated with the same marker in all the three plots. The output of the instrument radiometric model is also reported as a reference

© Author(s) 2026. CC BY 4.0 License.

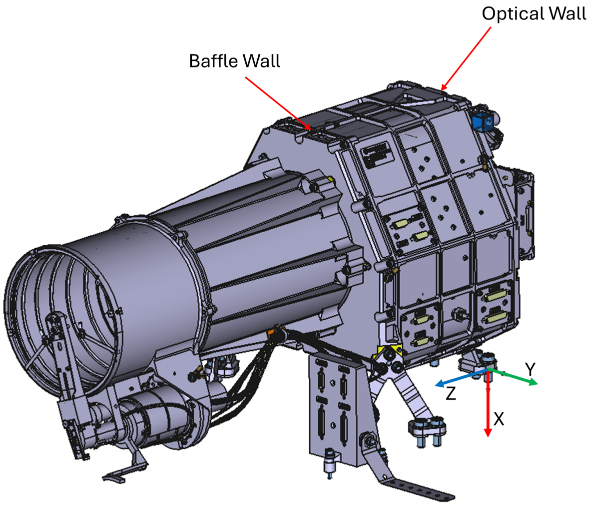

**Figure 23.** CAD drawing of JANUS. The JANUS reference system is shown over one of the three bipods, which is used as a mechanical reference. A variation of the thermal gradient between Baffle Wall and Optical Wall generates a rotation of the boresight around the y-axis

### 405 5.2.2 Attitude, Orbital Control System (AOCS) Errors

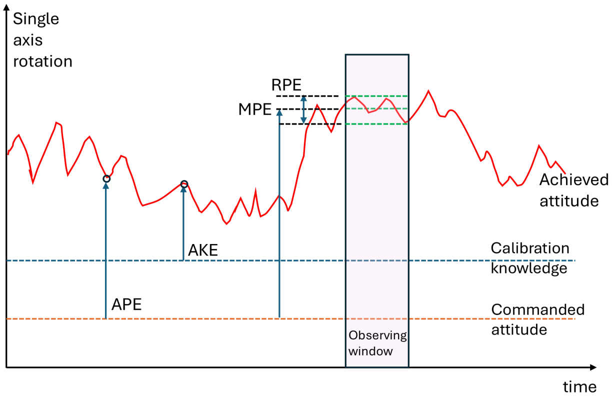

**Figure 24.** Visual depiction of some pointing errors parameters, as described in (ESSB-HB-E-003 Working Group, 2011)

The strategy described in section 4.1 to derive the extrinsic matrix (that is the orientation of the camera with respect to another reference system) has been limited to a single measure, i.e. a specific moment. According to (ESSB-HB-E-003 Working Group, 2011), two error sources should also be considered to refine the measurement:

- Absolute Knowledge Errors (AKE)

https://doi.org/10.5194/egusphere-2026-2032
Preprint. Discussion started: 14 April 2026
© Author(s) 2026. CC BY 4.0 License.

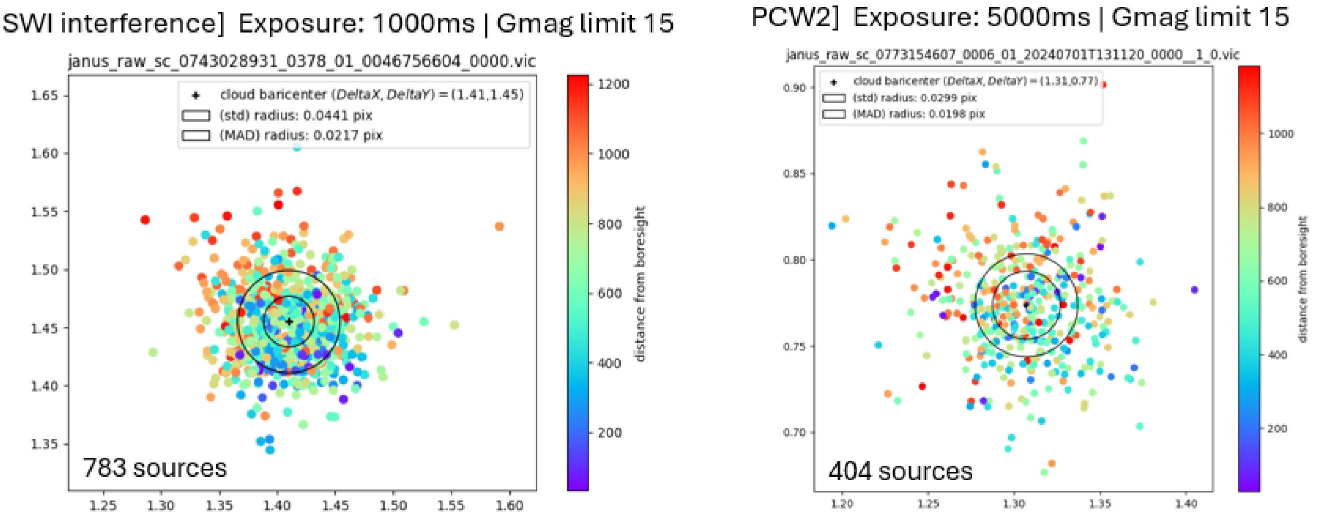

**Figure 25.** Residuals of the geometrical calibration applied to two star fields different from the one used for geometrical calibration. Units are JANUS pixels. For both measurements, the number of stars used to calculate the residual, the GAIA magnitude (Gmag) used to limit the queried stars and the exposure time are reported. The circles represent the standard deviation and the median absolute deviation (MAD). **left**: acquisition during an interference test with SWI. **right** acquisition during the second PCW.

– Relative Performance Errors (RPE)

A visual interpretation of these parameters of interest is provided in Figure 24

The first error to be considered is the AKE, that is the difference between the current knowledge of the attitude and the *real* one. For JANUS geometric calibration, this means that applying the procedure described in section 4.1 to a single image generates a rotation matrix which includes the error that the spacecraft AOCS commits in the reconstruction of the attitude. We used for this analysis, the *juice_ops* metakernel (ESA SPICE Service).

This can be seen in Figure 26 and 25. To perform a verification of the geometrical calibration, the JANUS geometrical model has been applied to two star fields differently with respect to the one used for the parameter determination. The only consideration here is that the distortion matrices describe the deviation of the distorted point with respect to the ideal case in contrast to the geometrical registration procedure that requires modeling of the ideal coordinates with respect to the distorted case. Both distortion matrix forms are derived in the same run by swapping the dependent and independent variables. Figure 26 shows the effect of numerically correcting the offset estimated by the cloud of points in Figure 25 for all the star coordinates of the field. The agreement is good, although there is a fixed offset which is attributed to the AKE in the *ops* kernel which contains the measured attitude as reconstructed by AOCS. A similar reasoning could be applied to the fact that during an observing window, even if inertial pointing is requested, the spacecraft has an unavoidable residual oscillation which is detectable by JANUS. For these reasons, in the next releases we will try to consider information from multiple acquisitions, in different time frames, to filter out the noise contribution and determine the actual attitude of the JANUS reference frame with respect to the

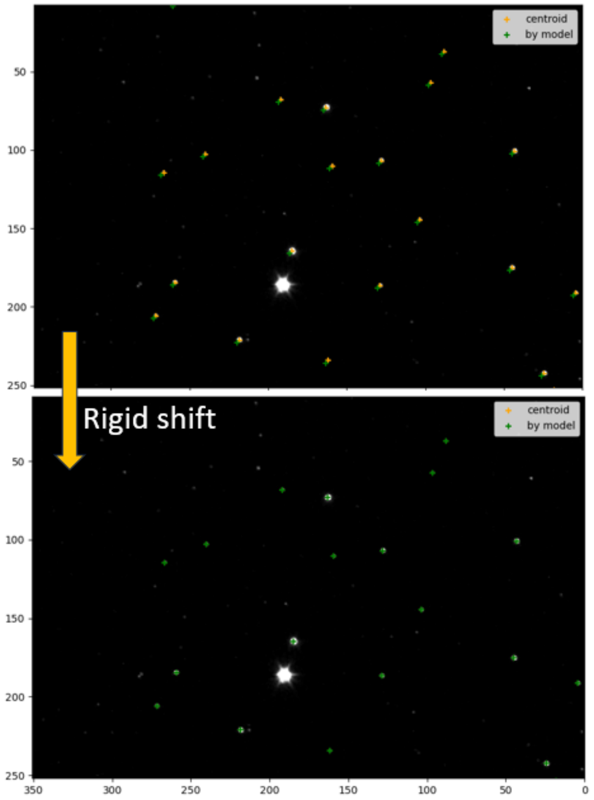

**Figure 26.** Example of the effect to correct all the star coordinates by the rigid offset. The relative positions of the simulated positions are coherent with the centroid ones. The rigid shift is performed by a simple subtraction of the offset deltas from the coordinates. The edge of the detector has been selected to see the quality of the reconstruction even in regions with the highest distortion

JUICE frame, which is meant to be independent of time. To be precise, as described in section 5.2.1 this is true only if all measurements are acquired in the same thermal environment, and therefore this aspect will also be taken into account.

## 6 Conclusions

JANUS successfully executed the science planning (Tubiana et al., this issue) as designed, with a high-quality dataset (204 lunar, 173 terrestrial, and 84 of the Moon-Earth system), resulting in a broad range of different inputs for testing the calibration process we developed for the instrument, more similar to the mission phase when extended resolved bodies will be observed. Noteworthy, the LEGA dataset provided also fundamental information for both cross-calibration with other instruments aboard JUICE (Langevin et al. (this issue),Nishiyama et al. (2026)) and feedback on the validity of the JANUS products, providing to be an excellent complement to the stellar observations performed during PCW. In this work, we showed the status of development of the calibration pipeline both in terms of radiometric and geometric aspects and the current limitations of our

**Table A1.** Images

| Figure | Image ID | Level |
|---|---|---|
| 3 | 0773155207_0168_01_20240701*t*135631 | raw |
| 6 left | 0777417466_0116_12_20240819*t*212320 | par |
| 6 right | 0777417466_0116_12_20240819*t*212320 | cal |
| 11 | 0779190669_0000_01_20240909*t*095142 | par |
| 12 | 0779190669_0000_01_20240909*t*095142 | par |
| 13 | 0777417466_0179_01_20240819*t*212617 | par |
| 15 | 0777417466_0190_01_20240819*t*213226 | par |
| 16 | 0779190669_0005_01_20240909*t*095144 | par |
| 19 | 0779190669_0015_03_20240909*t*095223 | par |
| 20 | 0779190909_0027_12_20240909*t*095703 | par |
| 25 left | 0743028931_0378_01_20230718*t*215455 | par |
| 25 right | 0773154607_0006_01_20240701*t*131120 | par |
| 26 | 0743028931_0378_01_20230718*t*215455 | par |

process. From the preliminary assessment resulting from the analysis of the LEGA data (Lucchetti et al. (this issue), Hueso et al. (this issue), Langevin et al. (this issue)), the JANUS calibration pipeline provides good results, without major issues. The LEGA experience provide us a better understanding of the impact the open points have on the accuracy of the JANUS products pushing a step forward the generation of high quality calibrated data required for the investigation of Ganymede and the Jupyter system.

*Data availability.* JANUS data are in the team proprietary period until the data release through ESA Planetary Science Archive (PSA). The first delivery of JUICE cruise data to PSA will occur in 2029.

## Appendix A

The Table A1 provides the reference for the images used in this work. The *Figure* column indicates the numbering of the Figure in this paper, the *Image ID* indicates the unique ID of the JANUS images, the *level* column indicates the level of the radiometric calibration pipeline used.

*Author contributions.* L. Agostini led the analysis and wrote the paper, K.-D. Matz led the geometric registration procedure. C. Tubiana led the instrument science operations and contributed to the on-ground calibration. V. Della Corte, A. Aboudan, T Bilotta, F. Sarti, S. Hviid, S. Mottola contributed to on-ground calibration. L. Penasa A. Aboudan, A. Dietz, R. Evill and I. Belgacem worked on science operations. M.

Aye led the calculation of exposure times. R. Hueso led the investigation of Earth LEGA data. A. Lucchetti led the investigation of Moon LEGA data. M. Read and M. R. Patel investigated the SDBS effect. E. Kersten, J.F. Bell III, A.Zinzi, J.M.C. Marin,L. M. Lara T. Roatsch and N. Schmitz worked on additional aspects of the investigation. R. Politi developed the code of the radiometric calibration pipeline and contributed to archiving. G. Portyankina played a key role in team coordination. P. Palumbo led the conceptualization of the investigation, data acquisition, algorithm development, and team coordination. All authors critically reviewed and revised the manuscript and approved the final version for publication.

*Competing interests.* The authors declare no competing interests.

*Acknowledgements.* PI and Italian team members acknowledge ASI support in the frame of ASI-INAF agreement n.2023-6-HH.0. R. Hueso was supported by Grant PID2023-149055NB-C31 funded by MICIU/AEI/10.13039/501100011033 and FEDER, UE.

JUICE is a mission under ESA leadership with contributions from its Member States. JANUS has been funded by the respective Space Agencies: ASI (lead funding agency), DLR, Spanish Research Ministry and the UK Space Agency.

This work has made use of data from the European Space Agency (ESA) mission *Gaia* (https://www.cosmos.esa.int/gaia), processed by the *Gaia* Data Processing and Analysis Consortium (DPAC, https://www.cosmos.esa.int/web/gaia/dpac/consortium). Funding for the DPAC has been provided by national institutions, in particular the institutions participating in the *Gaia* Multilateral Agreement.

© Author(s) 2026. CC BY 4.0 License.

## References

Agostini, L.: Characterization and calibration of VIS cameras for space applications-JANUS and HYPSOS systems, Ph.D. thesis, Università degli studi di Padova, available at https://hdl.handle.net/20.500.14242/98393, 2023.

Barker, M., Mazarico, E., Neumann, G., Zuber, M., Haruyama, J., and Smith, D.: A new lunar digital elevation model from the Lunar Orbiter Laser Altimeter and SELENE Terrain Camera, Icarus, 273, 346–355, 2016.

Da Deppo, V., Simioni, E., Naletto, G., and Cremonese, G.: Distortion definition and correction in off-axis systems, in: Optical Systems Design 2015: Optical Design and Engineering VI, vol. 9626, pp. 806–817, SPIE, 2015.

ESA SPICE Service: JUICE Operational SPICE Kernel Dataset, https://doi.org/10.5270/esa-ybmj68p, https://doi.org/10.5270/esa-ybmj68p, eSA SPICE Service.

ESSB-HB-E-003 Working Group: ESA pointing error engineering handbook, European Space Agency (ESA), Noordwijk, Netherlands, issue 1, revision 0 edn., reference: ESSB-HB-E-003, 2011.

Fest, E.: Stray light analysis and control, 2013.

Grasset, O., Dougherty, M., Coustenis, A., Bunce, E., Erd, C., Titov, D., Blanc, M., Coates, A., Drossart, P., Fletcher, L., et al.: JUpiter ICy moons Explorer (JUICE): An ESA mission to orbit Ganymede and to characterise the Jupiter system, Planetary and Space Science, 78, 1–21, 2013.

Hartley, R. and Zisserman, A.: Multiple view in Computer Vision, 2nd edtion, 2004.

Hueso, R., Antuñano, A., Lara, L. M., Stephan, K., Zinzi, A., Coustenis, A., Yair, Y., Sato, M., Haruyama, J., Simon, A., Tubiana, C., Penasa, L., Agostini, L., Lucchetti, A., Aboudan, A., Aye, M., Kersten, E., Matz, K.-D., Politi, R., Trauthan, F., Evill, R., Belgacem, I., Yukihiro, T., Castro-Marin, J. M., Della Corte, V., Hviid, S., Roatsch, T., Schmitz, N., Patel, M., Portyankina, G., and Palumbo, P.: JUICE-JANUS observations of Earth in preparation for the JANUS investigation of Jupiter's atmosphere, this issue.

Langevin, Y., Rodriguez, S., Guerlet, S., Poulet, F., Piccioni, G., Agostini, L., Armante, R., D'Aversa, E., Filacchione, G., Fletcher, L., Oliva, F., Royer, C., Seignovert, B., Stephan, K., Tosi, F., and Trent, T.: Post launch spectral and radiometric performances of MAJIS, the VIS-NIR imaging spectrometer of JUICE, this issue.

Liang, C.-K., Chang, L.-W., and Chen, H. H.: Analysis and compensation of rolling shutter effect, IEEE transactions on image processing, 17, 1323–1330, 2008.

Lucchetti, A., Massironi, M., Gwinner, K., Kenkmann, T., Penasa, L., Baby, N. R., Rotzoll, L., Karagoz, O., Rizos, J. L., Pajola, M., Tosi, F., Fornasier, S., Tusberti, F., Stephan, K., Pozzobon, R., Suarez-Valencia, J. E., Cagnin, D., Zambon, F., Chiarolanza, G., Coustenis, A., Giacomini, L., Hauber, E., Marchi, S., Matteoni, P., Mitri, G., Rossi, C., Hueso, R., Aboudan, A., Agostini, L., Kersten, E., Matz, K. D., Politi, R., Trauthan, F., Tubiana, C., Aye, M., Zinzi, A., Evill, R., Belgacem, I., Castro-Marin, J. M., Della Corte, V., Hviid, S., Roatsch, T., Schmitz, N., Lara, L. M., Patel, M. R., Portyankina, G., Palumbo, P., and Team, J.: Morphological and Spectrophotometric exploitation of JANUS LEGA Dataset: Langrenus impact crater characterization and evolution of the highland "isthmus" between Mare Fecunditatis and Mare Tranquillitatis, this issue.

MODTRAN: MODTRAN, https://www.nrel.gov/grid/solar-resource/spectra#paneld14e140_1.

Munari, M., Magrin, D., Greggio, D., Agostini, L., Lucchetti, A., Paolinetti, R., Barilli, M., Turella, A., Dattolo, A., Colosimo, A., et al.: StrayLight analysis update of Janus, the ESA mission JUICE camera, in: Space Telescopes and Instrumentation 2024: Optical, Infrared, and Millimeter Wave, vol. 13092, pp. 2408–2413, SPIE, 2024.

© Author(s) 2026. CC BY 4.0 License.

Nishiyama, G., Stark, A., Matz, K.-D., Hüttig, C., Wickhusen, K., Agostini, L., Althaus, C., Binger, J., Enya, K., George, J., Lingenauber, K., Kimura, J., Kobayashi, M., Macrì, G., Neumann, W., Penasa, L., Portyankina, G., Tubiana, C., Wilner, K., Palumbo, P., and Hussmann, H.: In-flight receiver calibration of the Ganymede Laser Altimeter (GALA) by passive Earth observations, EGUsphere, 2026, 1–24, https://doi.org/10.5194/egusphere-2026-520, 2026.

Palumbo, P., Roatsch, T., Lara, L., Castro-Marin, J., Della Corte, V., Hviid, S., Jaumann, R., Michaelis, H., Patel, M., Portyankina, G., et al.: The JANUS (Jovis Amorum ac Natorum Undique Scrutator) VIS-NIR multi-band imager for the JUICE mission, Space Science Reviews, 221, 32, 2025.

Photon Engineering, LLC: FRED Optical Engineering Software, https://photonengr.com/fred-software, versione [inserisci versione, es. 23.10], 2026.

Poulet, F., Piccioni, G., Langevin, Y., Dumesnil, C., Tommasi, L., Carlier, V., Filacchione, G., Amoroso, M., Arondel, A., D'Aversa, E., et al.: Moons and jupiter imaging spectrometer (MAJIS) on jupiter icy moons explorer (JUICE), Space Science Reviews, 220, 27, 2024.

Prusti, T., De Bruijne, J., Brown, A. G., Vallenari, A., Babusiaux, C., Bailer-Jones, C., Bastian, U., Biermann, M., Evans, D. W., Eyer, L., et al.: The gaia mission, Astronomy & astrophysics, 595, A1, 2016.

Simioni, E., Da Deppo, V., Re, C., Slemer, A., Capria, M. T., Ficai Veltroni, I., Borrelli, D., Dami, M., Tommasi, L., Mugnuolo, R., Amoroso, M., Longo, F., and Cremonese, G.: SIMBIO-SYS/STC stereo camera calibration: Geometrical distortion, Review of Scientific Instruments, 90, 043 106, https://doi.org/10.1063/1.5085710, 2019.

Soman, M., Holland, A. D., Stefanov, K. D., Gow, J. P., Leese, M., Pratlong, J., and Turner, P.: Design and characterisation of the new CIS115 sensor for JANUS, the high resolution camera on JUICE, in: High Energy, Optical, and Infrared Detectors for Astronomy VI, vol. 9154, pp. 64–74, SPIE, 2014.

Teledyne e2v: CIS115 Back-Illuminated CMOS Image Sensor, Teledyne e2v (UK) Limited, version 2 edn., https://www.teledyneimaging.com/media/1359/cis115.pdf, document A1A-785580, 2017.

Toledano, C., Taylor, S., Barreto, Á., Adriaensen, S., Berjón, A., Bialek, A., González, R., Woolliams, E., and Bouvet, M.: LIME: Lunar Irradiance Model of ESA, a new tool for absolute radiometric calibration using the Moon, Atmospheric Chemistry and Physics, 24, 3649–3671, 2024.

Tubiana, C., Penasa, L., Agostini, L., Palumbo, P., Aboudan, A., Aye, M., Matz, K.-D., Read, M., Bilotta, T., Hueso, R., Kerstin, E., Lara, L. M., Lucchetti, A., Politi, R., Trauthan, F., and Zinzi, A.: Planning of the JUICE/JANUS camera observations during the first ever Lunar-Earth Gravity Assist, this issue.

Turella, A., Della Corte, V., Paolinetti, R., Palumbo, P., Amoroso, M., Castronuovo, M., and Mugnuolo, R.: Structural-Thermal-Optical-Performance (STOP) analysis for the prediction of the line-of-sight stability of JANUS camera on board JUICE ESA mission, in: Optical Modeling and System Alignment, vol. 11103, pp. 101–112, SPIE, 2019.

Turella, A., Della Corte, V., Palumbo, P., Amoroso, M., Mugnuolo, R., and Noci, G. E.: JANUS Optical Head Line of Sight Temperature dependence Characterization and Validation by on ground test, in: 2021 IEEE 8th International Workshop on Metrology for AeroSpace (MetroAeroSpace), pp. 442–447, IEEE, 2021.

Vallenari, A., Brown, A. G., Prusti, T., De Bruijne, J. H., Arenou, F., Babusiaux, C., Biermann, M., Creevey, O. L., Ducourant, C., Evans, D. W., et al.: Gaia data release 3-summary of the content and survey properties, Astronomy & Astrophysics, 674, A1, 2023.